

Energy-distributable waterborne acoustic launcher for directional sensing

Tian Yang(杨天), Wenting Gao(高文婷), Shida Fan(范世达), Jie Ren(任捷), and Tianzhi Yang(杨天智)
Citation: Chin. Phys. B, 2023, 32 (**12**): 124302. DOI: 10.1088/1674-1056/acf5cf
Journal homepage: http://cpb.iphy.ac.cn; http://iopscience.iop.org/cpb

What follows is a list of articles you may be interested in

Method for measuring the low-frequency sound power from a complex sound source based on sound-field correction in a non-anechoic tank

Hongzhe Xu(徐宏哲), Qi Li(李琪), Rui Tang(唐锐), and Dajing Shang(尚大晶)
Chin. Phys. B, 2023, 32 (**5**): 054303. DOI: 10.1088/1674-1056/acb75c

Effects of mesoscale eddies on the spatial coherence of a middle range sound field in deep water

Fei Gao(高飞), Fang-Hua Xu(徐芳华), and Zheng-Lin Li(李整林)
Chin. Phys. B, 2022, 31 (**11**): 114302. DOI: 10.1088/1674-1056/ac6014

Parallel optimization of underwater acoustic models: A survey

Zi-jie Zhu(祝子杰), Shu-qing Ma(马树青), Xiao-Qian Zhu(朱小谦), Qiang Lan(蓝强), Sheng-Chun Piao(朴胜春), and Yu-Sheng Cheng(程玉胜)
Chin. Phys. B, 2022, 31 (**10**): 104301. DOI: 10.1088/1674-1056/ac7ccc

Wave mode computing method using the step-split Padé parabolic equation

Chuan-Xiu Xu(徐传秀) and Guang-Ying Zheng(郑广赢)
Chin. Phys. B, 2022, 31 (**9**): 094301. DOI: 10.1088/1674-1056/ac6940

Analysis of underwater decoupling properties of a locally resonant acoustic metamaterial coating

Ling-Zhi Huang(黄凌志), Yong Xiao(肖勇), Ji-Hong Wen(温激鸿), Hai-Bin Yang(杨海滨), Xi-Sen Wen(温熙森)
Chin. Phys. B, 2016, 25 (**2**): 024302. DOI: 10.1088/1674-1056/25/2/024302

Energy-distributable waterborne acoustic launcher for directional sensing

Tian Yang(杨天)[1], Wenting Gao(高文婷)[2], Shida Fan(范世达)[1], Jie Ren(任捷)[2], and Tianzhi Yang(杨天智)[1,†]

[1] *School of Mechanical Engineering and Automation, Northeastern University, Shenyang* 110819, *China*

[2] *Center for Phononics and Thermal Energy Science, Shanghai Key Laboratory of Special Artificial Microstructure Materials and Technology, School of Physics Sciences and Engineering, Tongji University, Shanghai* 200092, *China*

(Received 24 May 2023; revised manuscript received 24 August 2023; accepted manuscript online 1 September 2023)

Highly directional launch and intensity adjustment of underwater acoustic signals are crucial in many areas such as abyssal navigation, underwater signal communication, and detection for marine biology. Inspired by the phenomenon that aquatic animals like dolphins detect and track prey with high resolution, we propose an energy-distributable directional sensing strategy which can achieve parallel needle-like transmitting sound beams with adjustable energy based on out-coupling valley-polarized edge states. The acoustic spin angular momentum and energy flow distribution at different interfaces inside the phononic crystal are provided and they show tight coupling. Furthermore, a sound beam with a width of 20° and an acoustic intensity enhancement factor ≈ 6.6 are observed in the far field. As an application, we show that this device can be used as an acoustic energy distributor. This communication pattern with excellent functionalities and performance provides a desirable idea for high-energy-level directional collimated underwater sensing and underwater acoustic energy distribution.

Keywords: underwater sound, acoustic sensing and acquisition, metamaterials

PACS: 43.30.+m, 43.60.Vx, 78.67.Pt **DOI:** 10.1088/1674-1056/acf5cf

During the last decades, significant advances have been achieved in metasurfaces.[1–10] More recently, waterborne acoustic metasurfaces have received extensive interest. Exotic waterborne acoustic behaviors have been observed successively.[11,12] However, superdirectional underwater acoustic signal transmission remains a great challenge due to the strong fluid-solid interaction (FSI). Previous waterborne acoustic lens equipment has many defects such as large acoustic beam side lobes and poor noise immunity. Hence, a novel device that can overcome the drawbacks of traditional underwater acoustic techniques and the limitations of the FSI is urgently needed to be developed. In recent years, derived from research on condensed-matter physics, quantum-like effects in topological acoustic systems have been widely noticed,[13–18] such as acoustic spin.[18–21] Many exotic acoustic behaviors can be predicted to depend on the distribution of acoustic spin. In addition, superdirectional airborne and waterborne acoustic transmission which overcome the limitations of beamwidth and effective frequency range have been realized recently.[7,22,23] However, waterborne acoustic power distribution and the prediction of superdirectional behavior still need further discussion based on waterborne phononic crystals (PCs).

In this paper, we apply a design of the valley-hall topology insulator (VHTI) to underwater acoustic communication and propose a directional waterborne topology acoustic launcher (WTAL) with an energy distribution function as shown in Fig. 1.[16,24–26] Unlike airborne environments, the FSI is significantly evident in water. To obtain a large relative elastic modulus of the unit cells against the FSI, stainless steel (ASTM 1045) was selected to build WTALs. The material properties of the unit cells are listed in Table 1. Emitted parallel needle-like acoustic beams are received only by target audiences. Remarkably, the width of the output path is so narrow that the signal is not leaked to non-target listeners. Furthermore, the acoustic spin angular momentum and energy flow distribution at different interfaces inside the phononic crystal are provided and they show tight coupling. Energy changes in different sound paths can be achieved by simply adjusting the internal structure of the WTALs. In this sense, superdirectional acoustic energy distribution can be achieved based on such a platform with multiple tunable sound channels.

Table 1. Material properties.

Materials	Elastic modulus E (GPa)	Poisson's ratio ν	Mass density ρ (kg·m^{-3})
Steel	205	0.28	7850

As the acoustic kagome lattice PnC shown in Fig. 1, gray areas represent the topological order origin with the C_3 spatial symmetry. To induce the topological phase transition, the C_6 symmetry is reduced by modulating the hopping amplitude e. Here, the kagome lattices are constructed of the trimers where the lattice constant $a = 30$ mm, the edge length of strictly symmetric trimer $b = 19.9$ mm, and $e = 0.9$ mm. The model

†Corresponding author. E-mail: yangtianzhi@me.neu.edu.cn

© 2023 Chinese Physical Society and IOP Publishing Ltd

and simulations are performed by the finite element software COMSOL Multiphysics. In this regime, two different valley states of the acoustic trimer located at the topological order origin (rotation angle $\theta = 0°$) intersect at the Dirac point in Fig. 2(a). To transform the topological modes and initiate edge states, lattice deformations are introduced to break the C_6 symmetry in time-reversal (TR) invariant systems. Specifically, two reversible topological phases are realized via rotating the acoustic trimers. As shown in Fig. 2(a), similar to the energy band inversion effect, two opposite valley states take place, corresponding to $\theta = \pm 30°$, and the opening of the Dirac cone is observed. As a result of the topological transition in PnC with $\theta \neq 0°$, a separated band gap of 26.3–30.3 kHz (the widening of the band gap is discussed in supplementary material I) appears at the corner of the first Brillouin zone (BZ). It is worth noting that the yellow curves corresponding to the two band gaps with the acoustic spine shape represent opposite topological characteristics.

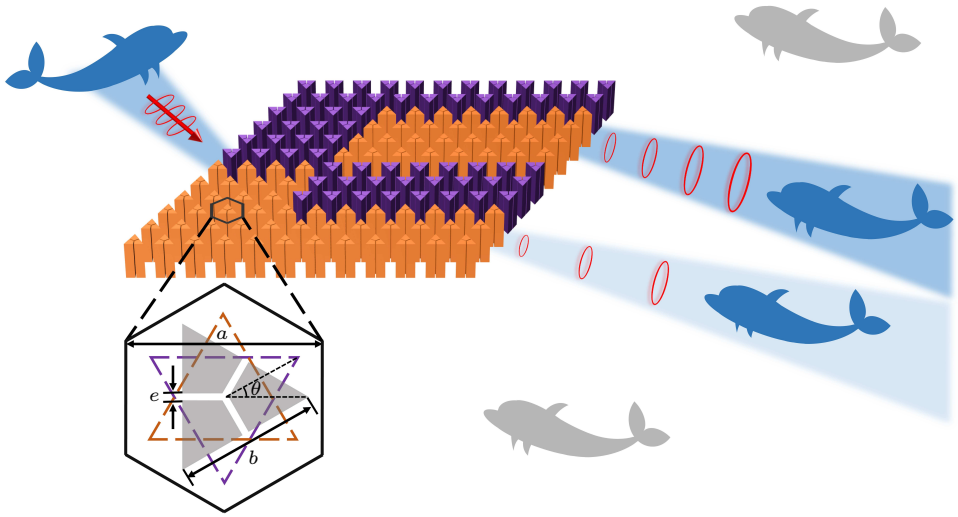


Fig. 1. Schematic diagram of WTALs with an energy distribution function. The sound signal is focused on a target audience and cannot be leaked to undesired listeners. The energy of the sound signals focused on different target audiences is tunable.

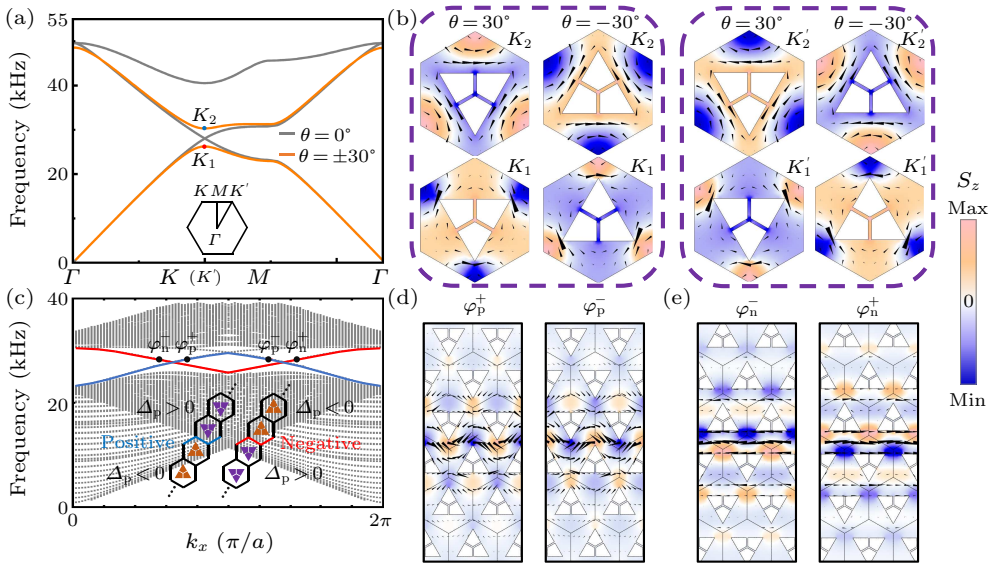


Fig. 2. Band inversion and the acoustic spin mode of the acoustic trimers. (a) With the rotation angle $\theta = 0°$, a Dirac cone appears. The band inversion effect takes place with $\theta = \pm 30°$. (b) The color indicates distributions of acoustic spin normalized according to the maximum absolute acoustic spin at K and K' points with $\theta = \pm 30°$. The unit of acoustic spin is kg·m^{-1}·s^{-1}. The black arrows represent the intensity and direction of energy flow. (c) Illustration of the dispersion relation of the superlattice. The blue (red) curve highlights the edge modes. Insets: the solid blue (red) line represents the positive-type (negative-type) interface. [(d), (e)] Illustrated distributions of energy flow and the acoustic spin normalized according to the maximum absolute acoustic spin at K and K' points along the positive- and negative-type interfaces, respectively.

To illustrate the topological mechanism, the effective Hamiltonian and valley-Chern indices are provided according to the first-order Kadomtsev–Petviashvili perturbation theory. Specifically, subjected to the limited number of eigenmodes, $H(\boldsymbol{k}_\perp) \equiv H(\delta\boldsymbol{k}) = v_D(\delta k_x \sigma_x + \delta k_y \sigma_y + m v_D \sigma_z)$ is an approximation, and m is the effective mass defined as $m = (\omega_{k_1^+} + \omega_{k_2^-})/(2v_D^2)$, where ω_k represents the band-edge frequency.[23] It is valid only in close proximity to the high-

symmetry K and K' points of the BZ, where v_D is the group velocity, σ_i $(i = x, y, z)$ are Pauli matrices of the valley states as the orbital degree of freedom, and $\delta\boldsymbol{k}$ is the distance from the Dirac points to the K (K') points, respectively.[27,28] By considering the TR symmetry, the effective Hamiltonian in the inequivalent K' point can be derived directly as $H(\delta\boldsymbol{k}') = v_D(-\delta k_x\sigma_x + \delta k_y\sigma_y + mv_D\sigma_z)$. The sign of the geometrical perturbation Δ_p is determined by the rotation angle of acoustic trimers. In other words, $\Delta_p < 0$ $(\Delta_p > 0)$ corresponds to $\theta = -30°$ $(30°)$. Furthermore, the non-vanishing valley-Chern indices can be expressed as $2C = \pm 1 \times \mathrm{sgn}(\Delta_p)$.[25,26,29] Considering the FSI, a large relative bulk elastic modulus of a trimer should be obtained after perturbation. It means that a large difference in elastic modulus between trimers and water is established. Otherwise, the relative elastic modulus of the trimers (e.g., resins, etc.) is so small that no topological band gap appears.

In Fig. 2(b), the acoustic spin distribution for all modes of the PCs are described. The acoustic spin can be quantitatively illustrated as $\boldsymbol{s} = \frac{\rho}{2\omega}\mathrm{Im}[v^* \times v]$, where ρ is the mass density, ω is the frequency, v is the particle vibration (acoustic) velocity, and v^* is the conjugate of v. Here, the acoustic spin is a spatial distribution rather than pure positive or negative values. In general, topological properties of the valley states at the K point are considered in focus, and the properties in the inequivalent K' point can be derived directly by considering the TR symmetry. The insets in Fig. 2(b) illustrate the intensity of the energy flow and the distributions of the acoustic spin at the valley states. For the erected trimers in the lattice, the lower boundary state of the acoustic spin is marked as K_1, and the higher boundary state is labeled as K_2. For an upside-down lattice, the state of the acoustic spin is the opposite to that in erected lattice. This is the micrometric basis of acoustic topological valley transport at the interface between two VHTIs. As shown in Fig. 2(c), the dispersion curves of both single ribbon-shaped superlattices separated by a zigzag interface are calculated. Notably, the zigzag interfaces are designed oppositely clearly. The positive-type (negative-type) interface is marked by a solid blue (red) line. As a key manifestation of the topological insulator, both spin-dependent one-way edge modes with opposite group velocities marked by blue and red lines are observed in the bulk band gap with the range from 26.3 kHz to 28.3 kHz. Figures 2(d) and 2(e) illustrate the distributions of the acoustic spin and energy flow in the positive- and negative-type interfaces. Obviously, the modes of different directions are of opposite acoustic spins in the acoustic spine interface, and the tight spin–momentum locking is observed in the topological system as previously verified in experiments.[20,21,30,31] Similar to the spin profile of the Gaussian beam of longitudinal acoustic wave, as shown in Ref. [17], the two sides of the acoustic beam transmitted along a zigzag interface have opposite spin distributions. Furthermore, the intensity of spin and energy density show a gradual debilitating trend on both sides.

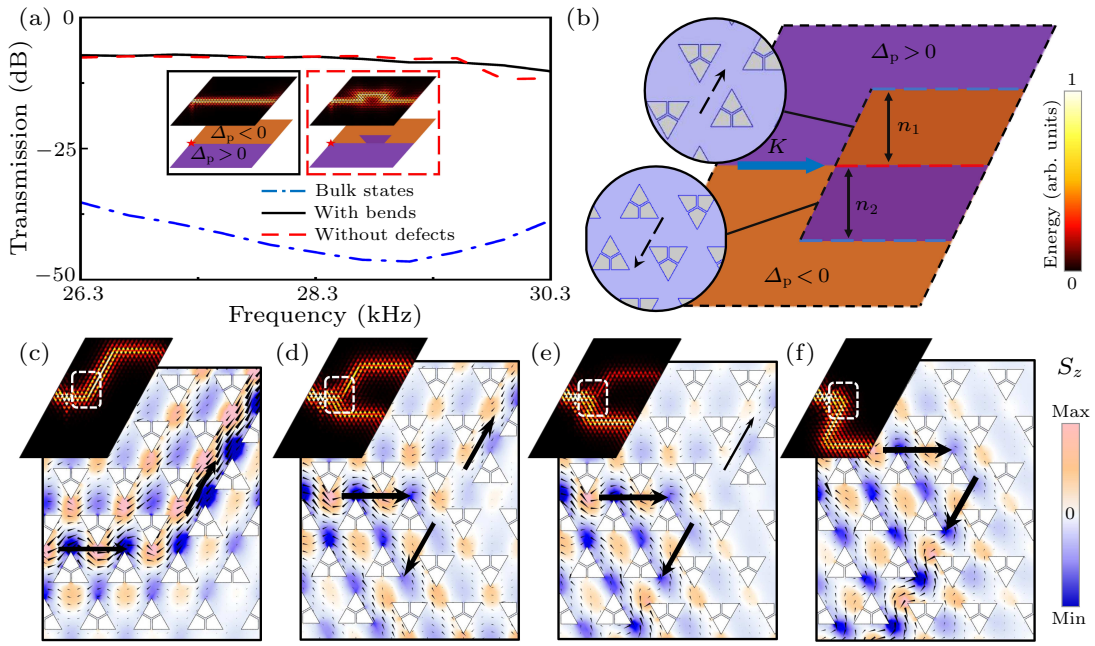


Fig. 3. Topologically protected edge states at the positive-type interfaces with K' valley polarization. (a) Transmission spectra of the topological valley transport with and without bends. Inset: simulated absolute pressure fields at the frequency $f = 28.3$ kHz. The point source is located at the purple pentagram. (b) The model of WTAL with double positive-type interfaces. Blue dashed lines and red dashed lines represent positive- and negative-type interfaces, respectively. Here n_1 and n_2 indicate the number of rows of upside-down and erected trimers, respectively. The blue arrows represent acoustic transmission paths. Insets: details of the interfaces leading to the upper and lower sound paths. (c), (d), (e), (f)] Distributions of acoustic spin and energy flow at $n_1 = 22$ $(n_2 = 2)$, $n_1 = 19$ $(n_2 = 5)$, $n_1 = 12$ $(n_2 = 12)$, and $n_1 = 2$ $(n_2 = 22)$, respectively.

On the one hand, the launching and out-coupling of the valley-polarized edge states are the pivotal mechanism of WTALs inside the PCs. Local edge states out of the bulk band gap are supported at the interface between two valley-Hall PCs with different valley polarization. As shown in the inset of Fig. 3(a), the topologically protected edge states of the straight and bent interfaces are observed. As an example, the two PCs are separated by a negative interface in a finite VHTI with $30a \times 30a$ unit cells. Only one valley polarized edge state propagates in the lock direction of the given valley, rested on an edge state at K' (K) point with $\Delta C = -1$ ($\Delta C = 1$). Sound topological valley transport with remarkable immunity effect is localized at the proximity of the interface. High transmission of sound waves is sustained across the topological band gap. However, the bulk states disappear from the topological band gap and the transmission is measured below -30 dB as shown in Fig. 3(a). Meanwhile, to observe the acoustic behavior of sound waves in multi-interface WTAL, two finite VHTIs connected in parallel at the right termination of the WTALs containing $60a \times 30a$ unit cells are established in Fig. 3(b). Both VHTIs are composed of 20 columns and n_i ($i = 1, 2$) rows, where n_i is natural numbers, and $n_1 + n_2 = 24$. A sound point source at 28.3 kHz is launched along the positive-type interface projected from the K' valley. Obviously, the positive-type interfaces are located above and below the two VHTIs, respectively. However, they are separated by a negative-type interface. It means that sound waves projected along the positive-type interface from the K' valley cannot pass through the negative-type interface between VHTIs from left to right. By varying n_1 and n_2, the distribution shift of the normalized energy fields and the acoustic spin are shown in Figs. 3(c)–3(f), sequentially. A clear and consistent variable trend of the acoustic spin and energy density is observed. It is noted that the types of interfaces leading to the upper and lower sound paths are different as shown in the insets of Fig. 3(b). The interface of the downward sound path is perfectly matched to the initial interface, while the match of the upward sound path is so poor relatively that a higher impedance is exhibited. As a result, approximate equal distribution does not appear at $n_1 = n_2 = 12$ in Fig. 3(e) but takes place at $n_1 = 19$ ($n_2 = 5$) in Fig. 3(d).

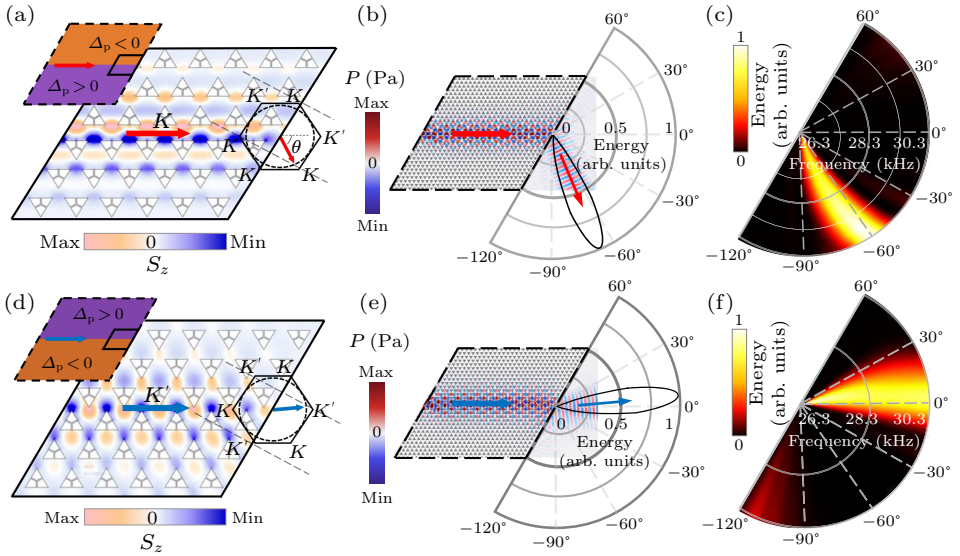


Fig. 4. Superdirectional sound radiation of the WTALs. [(a), (d)] Distribution of acoustic spin corresponding to K and K' valley-projected along the negative-type (positive-type) interface in k space at $f = 28.3$ kHz. A black solid hexagon indicates the 1st BZ and the black dashed circle represents the dispersion. [(b), (e)] Far-field distributions of normalized energy and sound pressure fields along the negative-type (positive-type) interface at $f = 28.3$ kHz. [(c), (f)] Normalized acoustical energy spectra in the range of 26.3–30.3 kHz.

On the other hand, the acoustic energy launches into free space directionally along the positive-type and negative-type out-coupled interfaces of the WTALs as illustrated in Fig. 4. The edge state guarantees reflection-free out-coupling which is essentially valley-projection. Moreover, whether inter-valley scattering is suppressed depends on the terminal type of the WTALs. A vanishing intervalley field overlap ensures that the undesired diffraction cannot take place at the zigzag termination of the WTALs.[26] Here, the radiation direction of the acoustic beam depends on the valley type of the projected edge state, which can be obtained according to the distribution of acoustic spin in Fig. 2. As shown in Figs. 4(a) and 4(d), the distribution of acoustic spin from left to right along the negative-type interface is consistent with the superlattice at φ_p^+ state which is projected from the K valley in Fig. 2(d). It means that the negative-type interface corresponds to the excitation from the K valley. Likewise, sound waves launched along the positive-type interface are projected from the K' valley. To obtain the refraction direction of the acoustic beam, the equifrequency curves in free space and

the BZ are plotted on the acoustic spine scale. Along the direction parallel to the terminal of WTALs, the component of the incident wavevector K (K') is matched with the frequency curve in free space owing to the momentum conservation parallel to the WTALs boundary. Specifically, the refraction angle at the frequency 28.3 kHz can be calculated by $\frac{4\pi}{3a} \times \cos 60^\circ = \frac{2\pi f}{c} \times \cos(120^\circ + \theta_-)$ to be $\theta_- = -66.08^\circ$. Likewise, the refraction angle can also be determined to be $\theta_+ = 6.08^\circ$ at the acoustic spine frequency for the WTALs with the positive-type interface.

To verify the prediction of the theoretical refraction angles, the far-field radiation patterns of WTALs with negative- and positive-type interfaces are scanned within an angular range shown in Figs. 4(b) and 4(e). The observed $\theta_- = -66^\circ$ and $\theta_+ = 6^\circ$ demonstrate indirectly that the out-coupled edge states obey the superdirectional selection rule of the valley projection. Positive (negative) angle acoustic refraction is completely suppressed by the WTAL with a negative-type (positive-type) interface. Furthermore, the far-field normalized energy spectra are observed across the entire frequency range of the topological band gap in Figs. 4(c) and 4(f). It means that functions of the proposed WTALs can be implemented between 28.3 kHz and 30.3 kHz. Additionally, three remarks need to be clarified: (1) The theoretical predictions are in great agreement with the simulation results. The small angular difference originates from the detection step of 1° during the simulation. (2) The half-energy beamwidth of the main lobe of WTALs with negative (positive) interfaces is 20° (14°) without side lobes. Protected and efficient energy transfer ensures that the sound can be focused on the target audience without being compromised. (3) The peak amplitudes of the far-field radiation of WTALs are about 6.63 times than the standard acoustic waveguides. Considering thermal adhesion effect of acoustic structures, the actual gain should be reduced than theoretical gain as shown in supplementary material Ⅱ. It implies that superdirectional transmission appears universally at considerable far-field sound levels.

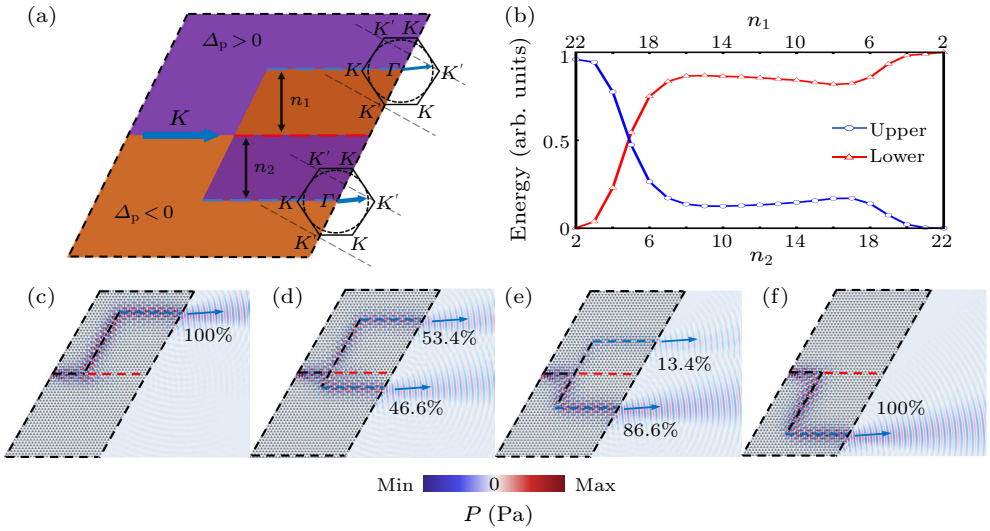


Fig. 5. The model of WTAL with double positive-type interfaces. (a) Demonstration of superdirectional acoustic energy distribution with tunable WTALs. (b) Relationships between the normalized energy of the upper and lower paths and the number of rows of inverted and vertical trimers. [(c), (d), (e), (f)] Distributions of acoustic pressure fields at $n_1 = 22$ ($n_2 = 2$), $n_1 = 19$ ($n_2 = 5$), $n_1 = 12$ ($n_2 = 12$), and $n_1 = 2$ ($n_2 = 22$), respectively, and marked with the energy percentage in each sound path.

Accurate superdirectional acoustic signal focusing not only is significant in underwater communication but also plays an important role in multi-channel acoustic information transmission. Considering both the internal and external characteristics of PCs, superdirectional acoustic energy distribution in parallel dual channels can be achieved with tunable WTALs in underwater acoustic environments. As illustrated in Fig. 5, a sound point source at 28.3 kHz is launched along the positive-type interface projected from the K' valley as an example. The WTAL is acoustic spine as the one shown in Fig. 3(b). As a result, parallel acoustic signals launched from the termination of the two positive-type interfaces can be obtained. Not only the two acoustic beams can be kept at a fixed interval relying on $n_1 + n_2 = 24$, but their energy distribution will be achieved by rotating the unit cells in a whole row to vary n_1 and n_2. Curves of the normalized energy distribution with n_i are shown in Fig. 5(b). Specifically, the distribution of the sound pressure fields with the energy shift trend are shown in Figs. 5(c)–5(f), sequentially. It is noted that equal distribution of energy does not take place at $n_1 = n_2 = 12$ in Fig. 5(e). As shown in the insets of Fig. 5(a), the types of interfaces leading to the upper and lower sound paths are different. The interface of the downward sound path is perfectly matched to the initial interface, while the match of the upward sound path is so poor relatively that a higher impedance is exhibited. Thus, the intersection point of the energy distribution curve appears on

one side instead of the middle in Fig. 5(b), and approximate equal distribution of energy takes place at $n_1 = 19$ ($n_2 = 5$) in Fig. 5(d). Similarly, acoustic energy distribution can also be realized by launching along the negative-type interface projected from the K valley. Rested on the above model, multi-channel sound energy distribution at different intervals can be realized, depending on the requirements of the actual application.

In summary, we propose directional WTALs with an energy distribution function based on valley-hall topological insulators, which not only launch parallel needle-like signals in a specific direction but also control the energy of the acoustic signal from different sound paths. Unlike airborne environments, the FSI is significantly evident in water. To obtain a large relative elastic modulus of the trimers against the FSI, ASTM 1045 was selected to build WTALs. The distributions of angular momentum and energy flow in different cases are observed. Furthermore, high energy level communication is realized, relying on out-coupling and sustaining of valley-polarized edge states. WTALs can not only radiate superdirectional acoustic beams with a width of less than 20° but also adjust their energy. The theoretical predictions and simulation results are in good agreement. In addition, the equipment is expected to be further optimized towards miniaturization and broadbanding in the future. Superdirectional WTALs provide a desirable idea for high-energy-level directional collimated underwater sensing and underwater acoustic energy distribution. In this sense, multi-level directional acoustic energy distribution can be achieved potentially based on such a platform with multiple tunable sound channels.

Acknowledgements

This work was supported by the National Natural Science Foundation of China (Grant Nos. 12232014 and 12072221) and the Fundamental Research Funds for the Central Universities (Grant No. 2013017).

References

[1] Guo Y, Li B and Yin X 2020 *Phys. Rev. Appl.* **13** 044009
[2] Zhao J, Cui X, Bonello B, Djafari-Rouhani B, Yuan W, Pan Y, Ren J, Zhang X and Zhong Z 2021 *J. Mech. Phys. Solids* **150** 104357
[3] Zhao J, Chen Z N, Li B and Qiu C W 2015 *J. Appl. Phys.* **117** 214507
[4] Zhu X, Ramezani H, Shi C, Zhu J and Zhang X 2014 *Phys. Rev. X* **4** 031042
[5] Shen Y, Zhu X, Cai F, Ma T, Li F, Xia X, Li Y, Wang C and Zheng H 2019 *Phys. Rev. Appl.* **11** 034009
[6] Zhao J, Li B, Chen Z and Qiu C W 2013 *Sci. Rep.* **3** 2537
[7] Lin H, Xu Z Q, Cao G, Zhang Y, Zhou J, Wang Z, Wan Z, Liu Z, Loh K P, Qiu C W, Bao Q and Jia B 2020 *Sci. Appl.* **9** 137
[8] Hou Z, Ding H, Wang N, Fang X and Li Y 2021 *Phys. Rev. Appl.* **16** 014002
[9] Yu G, Qiu Y, Li Y, Wang X and Wang N 2021 *Phys. Rev. Appl.* **15** 064064
[10] Yang T, Lin Z and Yang T 2023 *Adv. Eng. Mater.* **25** 200805
[11] Zhao J, Li B, Chen Z N and Qiu C W 2013 *Appl. Phys. Lett.* **103** 151604
[12] Zhu X, Huang G, Feng Z and Wu J 2019 *Sensors* **20** 186
[13] Zhang D, Ren J, Zhou T and Li B 2019 *New J. Phys.* **21** 093033
[14] Wen X, Qiu C, Qi Y, Ye L, Ke M, Zhang F and Liu Z 2019 *Nat. Phys.* **15** 352
[15] Lu J, Qiu C, Ke M and Liu Z 2016 *Phys. Rev. Lett.* **116** 093901
[16] Ye L, Qiu C, Lu J, Wen X, Shen Y, Ke M, Zhang F and Liu Z 2017 *Phys. Rev. B* **95** 174106
[17] Fan X, Xia T, Qiu H, Zhang Q and Qiu C 2022 *Phys. Rev. Lett.* **128** 216403
[18] Long Y, Ren J and Chen H 2018 *Proc. Natl. Acad. Sci. USA* **115** 9951
[19] Yang C, Tan Y T, Chen H and Ren J 2021 *J. Appl. Phys.* **129** 135106
[20] Long Y, Ge H, Zhang D, Xu X, Ren J, Lu M H, Bao M, Chen H and Chen Y F 2020 *Nat. Sci. Rev.* **7** 1024
[21] Long Y, Zhang D, Yang C, Ge J, Chen H and Ren J 2020 *Nat. Commun.* **11** 4716
[22] Zhang Z, Tian Y, Wang Y, Gao S, Cheng Y, Liu X and Christensen J 2018 *Adv. Mater.* **30** 1803229
[23] Zheng S, Duan G and Xia B 2020 *Int. J. Mech. Sci.* **174** 105463
[24] Zhu W, Long Y, Chen H and Ren J 2019 *Phys. Rev. B* **99** 115410
[25] Zhang F, MacDonald A H and Mele E J 2013 *Proc. Natl. Acad. Sci. USA* **110** 10546
[26] Ma T and Shvets G 2016 *New J. Phys.* **18** 025012
[27] Kane C L and Mele E J 2005 *Phys. Rev. Lett.* **95** 226801
[28] Peano V, Brendel C, Schmidt M and Marquardt F 2015 *Phys. Rev. X* **5** 031011
[29] Ezawa M 2013 *Phys. Rev. B* **88** 161406
[30] Shi C, Zhao R, Long Y, Yang S, Wang Y, Chen H, Ren J and Zhang X 2019 *Nat. Sci. Rev.* **6** 707
[31] Yuan W, Yang C, Zhang D, Long Y, Pan Y, Zhong Z, Chen H, Zhao J and Ren J 2021 *Nat. Commun.* **12** 6954